ACS APPLIED NANO MATERIALS

www.acsanm.org
Article

Individually Encapsulating Metal–Organic Frameworks in Partially Reduced Graphene Oxide to Enhance Electrical Conductivity While Preserving Porosity

Bo-Min Kim, Gun Woo Jang, Changhyun Ko, Kyung Min Choi, Won Ho Choi,* and Jeeyoung Shin*

Cite This: https://doi.org/10.1021/acsanm.5c02501
Read Online

ABSTRACT: The rational design of porous materials with high electrical conductivity is critical for optimizing their performance in energy-storage applications. In this study, we synthesize a partially reduced graphene oxide-encapsulated metal–organic framework (MOF) by following a facile self-assembly strategy to ensure intimate contact between the graphene oxide layer and the MOF while preserving the intrinsic porosity of the latter. Surface functionalization of the MOF with 3-aminopropyltriethoxysilane facilitates the controlled deposition of graphene oxide layers, preventing pore blockage and allowing uniform encapsulation. Unlike conventional MOF-based composites that suffer from pore blockage or agglomeration, this approach preserves open ion-diffusion pathways while enabling efficient charge transport. The encapsulated graphene layers exhibit a reduced number of oxygen functional groups and increased Csp^2 content, enhancing electron conductivity and structural stability. Characterization results confirm that partially reduced graphene oxide encapsulation preserves the microporous framework of the MOF, considerably enhancing its electrical conductivity while preserving its porosity.

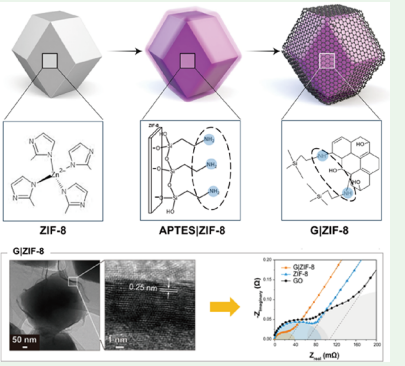

KEYWORDS: *encapsulation, metal–organic frameworks, zeolitic imidazolate frameworks, graphene oxide, self-assembly, 3-aminopropyltriethoxysilane, conductivity*

1. INTRODUCTION

Metal–organic frameworks (MOFs) intrinsically possess large surface areas and customizable pore architectures, and therefore, MOFs are highly attractive as electrode materials for electrochemical devices.[1] Despite these benefits, the poor electrical conductivities of MOFs limit their electrochemical application.[2] Various strategies have been explored to overcome this limitation, including the development of highly electrically conductive MOFs,[3,4] postsynthetic modifications to MOF structures,[5] and the synthesis of MOF composites by using alternative materials.[6] However, these strategies encounter certain problems. Conductive MOFs are limited by the availability of suitable metal species and ligands, whereas postsynthetic modifications involve complex processes. Although MOF composites also face challenges such as phase separation or agglomeration of the individual components, they are considered promising candidates because they can broaden the range of MOFs available. Yet, conventional mixing-based MOF composites rarely achieve uniform, particle-by-particle encapsulation; instead, they often result in partial coverage or stacked carbon shells around agglomerated MOFs, which can block pore windows and hinder electron transport. This limitation is further exacerbated by the intrinsically poor interfacial affinity of MOFs for other materials, arising from saturated coordination bonds and the typically hydrophobic nature of MOF surfaces. As a result, MOFs adhere weakly to conductive additives, thereby limiting the effectiveness of such composites.

To address these limitations, recent studies have explored strategies to integrate MOFs with conductive materials to enhance charge transport and overcome their intrinsic conductivity issues. For instance, creating intimate interfaces between MOFs and carbon networks can reduce charge transfer barriers while preserving porosity, and interfacial coupling between conducting polymers and MOFs has been shown to significantly improve electrochemical performance by mitigating the inherent conductivity limitations.[7,8] In this study, we improve the affinity of MOFs by introducing amine functional groups. Specifically, 3-aminopropyltriethoxysilane (APTES) is used to generate a chemically bonded interface between graphene oxide and the zeolitic imidazolate framework-8 (ZIF-8) (G|ZIF-8). This APTES-enabled self-assembly affords individual, particle-by-particle encapsulation of ZIF-8 by GO, a configuration that is rarely attainable with

Received: May 14, 2025
Revised: September 30, 2025
Accepted: October 1, 2025

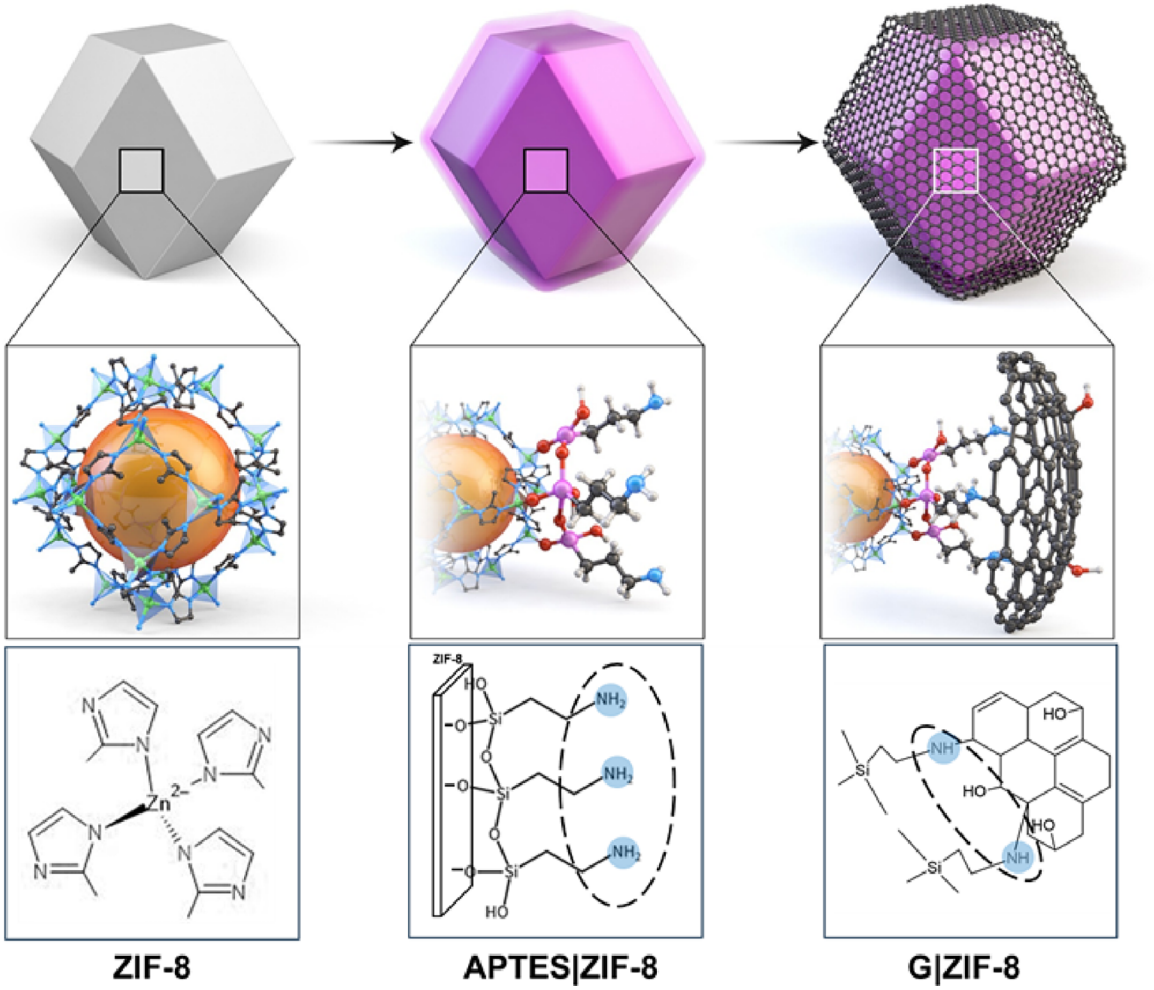

Figure 1. Schematic illustration depicting the synthesis processes of APTES|ZIF-8 and G|ZIF-8 on ZIF-8. Note: the sizes of APTES and graphene are enlarged for clarity.

conventional composites. This treatment maintains the integrity of the pore structure and enhances the electrical conductivity of G|ZIF-8. The propyl spacer in APTES helps minimize pore blockage and ensures robust GO−ZIF-8 interactions. Therefore, this approach preserves the large surface area and high porosity of ZIF-8. The resulting composite exhibits superior electrical conductivity and capacitance, demonstrating its potential for use as an advanced electrode material in energy storage applications. Our results highlight the potential of individual encapsulation strategies to overcome the limitations of MOFs, such as weak conductivity and poor material integration, by leveraging the surface functionalization and unique properties of graphene oxide.

2. RESULTS AND DISCUSSION

We selected ZIF-8 owing to its high microporosity, which increases its surface area substantially.[9] To impart ZIF-8 with conducting properties, we encapsulated it in graphene oxide while maintaining high microporosity. The encapsulation process followed to obtain G|ZIF-8 is illustrated in Figure 1. The self-assembly process was initiated by modifying the ZIF-8 surface with APTES (to obtain APTES|ZIF-8), which consists of an amino group ($-NH_2$), a propyl chain ($-C_3H_6-$), and a silane group ($-Si(OC_2H_5)_3$) (Figure S1). During the reflux step at 90 °C, hydroxyl groups (−OH) formed on the outer surface of ZIF-8, and APTES underwent hydrolysis ($-Si-(OC_2H_5)_3 \rightarrow Si-OH$).[10] The resulting silanols (Si−OH) condensed with newly generated surface − OH groups, forming surface anchored siloxane linkages (Si−O−Zn) that grafted APTES onto ZIF-8.[11−13] Subsequently, APTES|ZIF-8 was transferred to a graphene oxide (GO) solution. Such dispersions are typically mildly acidic to near-neutral (ca. pH 4−6). Under this condition, the terminal amines ($-NH_2$) on APTES are predominantly protonated ($-NH_3^+$) while GO carries a net negative surface charge. These complementary charges drive electrostatic self-assembly and conformal encapsulation, yielding G|ZIF-8. This process also prevents GO aggregation and preserves the intrinsic microporosity of ZIF-8.

The individually encapsulated G|ZIF-8 structure was observed using a scanning electron microscope (SEM) (Figure 2a). The SEM image of ZIF-8 revealed a smooth surface, whereas that of APTES|ZIF-8 exhibited a rough surface owing to the presence of APTES. Energy-dispersive X-ray spectroscopy (EDS) conducted on APTES|ZIF-8 confirmed the coordination of APTES to the ZIF-8 surface, as indicated by the presence of Si in the EDS maps (Figure S2). The SEM images of G|ZIF-8 revealed a wrinkled surface, indicating the attachment of the graphene layer to ZIF-8. In contrast, a physical mixture of GO and ZIF-8 prepared without APTES did not form a conformal coating and showed separate

https://doi.org/10.1021/acsanm.5c02501
ACS Appl. Nano Mater. XXXX, XXX, XXX−XXX

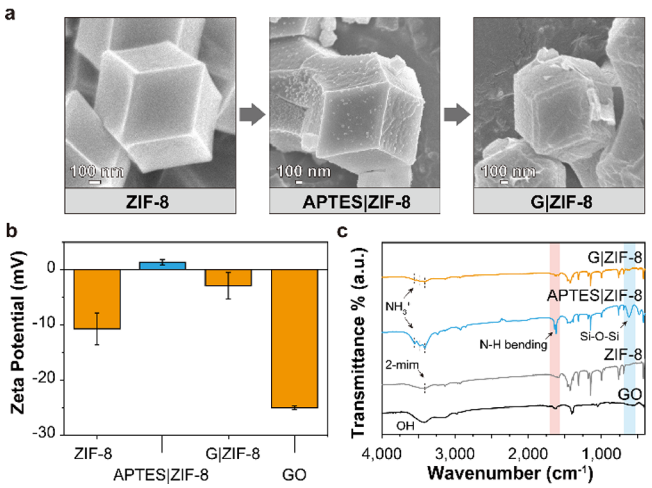

Figure 2. (a) SEM images revealing the processes followed for preparing G|ZIF-8; (b) zeta potential values; and (c) FTIR spectra of GO, ZIF-8, APTES|ZIF-8, and G|ZIF-8.

aggregates (Figure S3), indicating that APTES is essential for individual encapsulation.

Zeta potential measurements and Fourier-transform infrared (FTIR) spectroscopy revealed the encapsulation mechanism (Figures 2b and 2c). The measured zeta potential of pristine ZIF-8 was − 10.7 mV, consistent with an imidazolate-terminated surface, which generated a small negative charge. The zeta potential of APTES|ZIF-8 shifted to +1.4 mV, reflecting the surface grafting of APTES and the presence of $-NH_3^+$. This positive shift originates from the APTES hydrolysis and condensation with surface − OH groups, forming Si−O−Zn on APTES|ZIF-8. The FTIR spectrum of ZIF-8 indicated the presence of a secondary amine group, which possibly originated from the uncoordinated N in 2-mim (Figure S1). The FTIR spectrum of APTES|ZIF-8 contained three prominent peaks between 3300−3600 cm^{-1} and a strong absorption peak corresponding to the N−H bending mode at 1619 cm^{-1}, indicating the presence of a positively charged protonated amine group ($-NH_3^+$) on the surface. Additionally, a distinct peak was observed at 474 cm^{-1}, corresponding to the scissoring absorption mode of Si−O−Si, further verifying the successful attachment of APTES to the ZIF-8 surface. Upon encapsulation with GO, the zeta potential shifted back to a negative value of − 2.9 mV, confirming successful interaction between positively charged APTES|ZIF-8 and negatively charged GO.[14]

Transmission electron microscopy (TEM) imaging of G|ZIF-8 revealed wrinkled regions on the graphene layer encapsulating ZIF-8 (Figures 3a, S4, and S5) with a lattice fringe of approximately 0.25 nm and a hexagonal selected area electron diffraction pattern (Figure 3b). The lattice spacing of 0.25 nm is indexed to the in-plane {100} family of graphitic planes, and the hexagonal symmetry confirms the graphitic ordering in the encapsulating layer. This wrinkled morphology indicated that the GO sheets adhered conformally to the ZIF-8 surface, following the ZIF-8 structure rather than forming restacked GO aggregates. GO, which contains various functional groups such as carboxylic, hydroxyl, and epoxy,[15] can interact strongly with the $-NH_3^+$ groups on APTES-modified ZIF-8. These electrostatic interactions facilitate the close attachment of the GO sheets to the ZIF-8 surface.[16,17] However, complete surface sealing was prevented owing to the

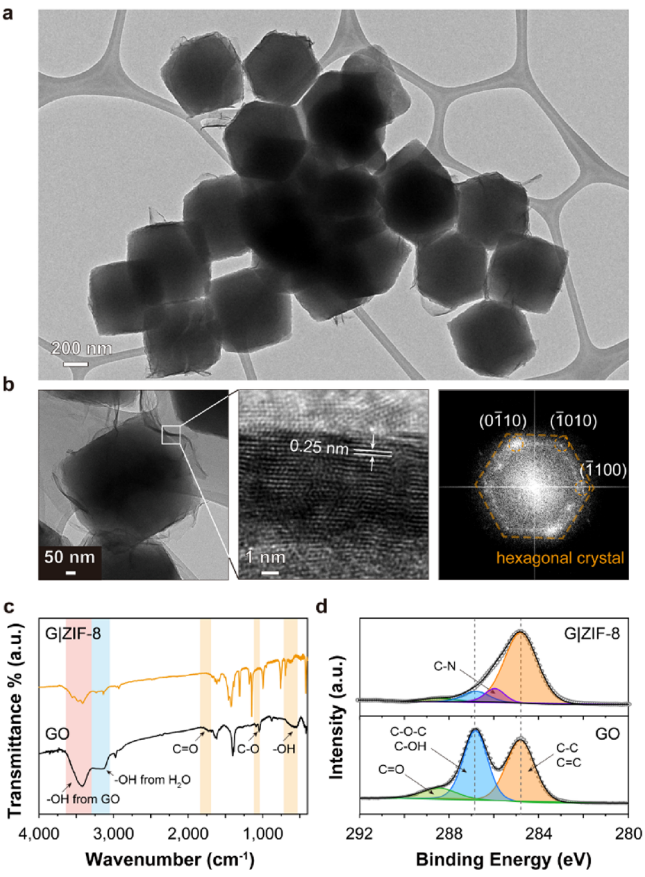

Figure 3. (a−b) Transmission electron microscopy (TEM) and high-resolution TEM images of G|ZIF-8; (c) comparison between the FTIR spectra of GO and G|ZIF-8; and (d) C 1s core level X-ray photoelectron spectra of GO and G|ZIF-8.

carbon chain length of APTES ($-C_3H_6-$), which introduced nanoscale interstitial voids between the GO layers and the MOF surface. These voids served as open ion-diffusion pathways, enabling electrolyte ions to access the internal pores of ZIF-8 despite the encapsulation.[18,19] The FT-IR spectra further demonstrated the structural changes caused by the attachment of the wrinkled graphene to G|ZIF-8 (Figure 3c). The spectrum of GO contained prominent peaks at 3418, 1630, and 1047 cm^{-1}, corresponding to the − OH, C = C, and C−O functional groups, respectively.[20] However, these peak intensities decreased substantially in the spectrum of G|ZIF-8, suggesting that the functional groups on GO were attenuated owing to strong interactions with the ZIF-8 surface during encapsulation. The results obtained from analyzing the C 1s XPS spectra further support the differences between the surface characteristics of GO and G|ZIF-8, as illustrated in Figures 3c, S6, and S7.[21−24] The spectrum of GO contained prominent peaks corresponding to epoxy or hydroxyl groups (286.82 eV) and carbonyl groups (288.48 eV). By contrast, the intensities of these peaks in the spectrum of G|ZIF-8 were weak. These reductions in peak intensities indicated a change in the surface chemical properties, that is, the characteristics of G|ZIF-8 were more similar to those of the reduced graphene oxide layers than those of the isolated GO sheets.[25]

The Raman spectra of GO and G|ZIF-8 are depicted in Figure S8. The spectra of GO and G|ZIF-8 contained peaks corresponding to the D (~1356 cm^{-1}) and G (~1598 cm^{-1}) bands, respectively. The relative intensity ratios (I_D/I_G) of the

https://doi.org/10.1021/acsanm.5c02501
ACS Appl. Nano Mater. XXXX, XXX, XXX−XXX

D and G bands were calculated to estimate the degree of graphitization of the carbonaceous materials.[26] For GO and G|ZIF-8, these ratios were 0.968 and 0.925, respectively, indicating that the ratio obtained for G|ZIF-8 was 0.043 lower than that obtained for GO. This decrease may be attributed to a reduction in structural defects due to increased G-band intensity. However, the introduction of sp^3-type defects via reactions between APTES amine groups and oxygen-containing functional groups on GO cannot be ruled out. These opposing effects—partial restoration of sp^2 domains and concurrent sp^3 defect formation—likely coexist in G|ZIF-8, resulting in a slight change in the observed I_D/I_G ratio.[27,28] Furthermore, the $(I_D/I_G)_F$ values were calculated by fitting a pseudo-Voigt function to assess the Csp^2 degree of GO.[29] The ratios for GO and G|ZIF-8 were 0.948 and 0.883, respectively, indicating that the ratio for G|ZIF-8 was lower than that for GO.

X-ray diffraction (XRD) patterns (Figure 4a) demonstrated the structural stability of G|ZIF-8 after encapsulation. The

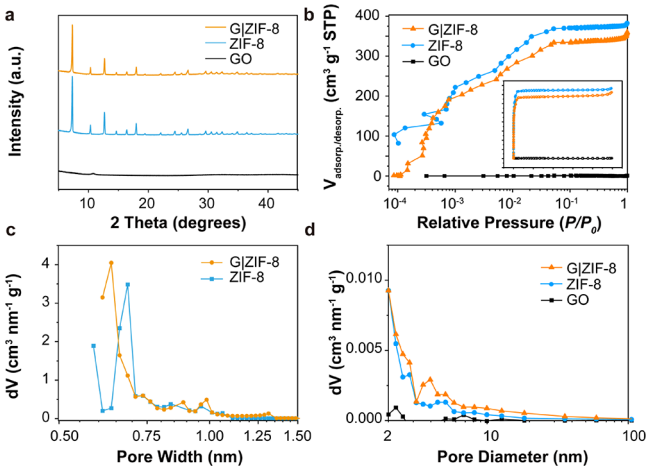

Figure 4. (a) Powder XRD patterns; (b) N_2 adsorption−desorption isotherms plotted on a logarithmic P/P_0 axis; inset: linear-scale view (P/P_0 = 0−1) (c) HK micropore size distribution plot; the *x*-axis major tick interval is set to 0.05 nm and (d) BJH pore size distribution curves of GO, ZIF-8, and G|ZIF-8.

peaks observed in the spectrum of G|ZIF-8 matched well with those in the spectrum of pristine ZIF-8,[30] indicating that the crystalline structure of ZIF-8 was preserved even after encapsulation. The absence of additional peaks or significant shifts suggested that the graphene layers interacted primarily with the surface rather than being integrated into the ZIF-8 crystal structure. The N_2 physisorption isotherms on a logarithmic P/P_0 axis are depicted in Figure 4b; this representation highlights the ultralow-pressure region, and the inset provides the conventional linear-scale view (P/P_0 = 0−1). Both ZIF-8 and G|ZIF-8 yielded type-I isotherms characterized by a steep adsorption region owing to strong adsorption, indicating the presence of a microporous structure.[31] By contrast, GO yielded a type-IV isotherm with a negligible hysteresis loop at high relative pressure, indicating the presence of slit-shaped pores formed by loose assemblies of plate-like particles.[32] The corresponding Brunauer−Emmett−Teller (BET) surface areas of ZIF-8, GO, and G|ZIF-8 were 1405, 5, and 1364 $m^2\ g^{-1}$, respectively. Despite the addition of GO with extremely small surface area, the surface area of G|ZIF-8 was only 3% less than that of ZIF-8, indicating that APTES treatment and graphene encapsulation preserved the integrity of the pore structure without causing pore blockages. The similarity between the FTIR spectra of ZIF-8 and G|ZIF-8 in the low-wavenumber region suggested that the ZIF-8 structure was preserved in G|ZIF-8. Micropore-size distributions were obtained by the HK method for ZIF-8 and G|ZIF-8 (Figure 4c; D ≤ 1.5 nm), and mesopore-size distributions by the BJH method for ZIF-8, G|ZIF-8, and GO (Figure 4d; D ≥ 2 nm). In the micropore range, the HK peak of G|ZIF-8 (0.755 nm) was slightly smaller than that of ZIF-8 (0.769 nm). This slight decrease in micropore size suggested that the microporous structure remained largely intact after APTES treatment. This result confirmed that G|ZIF-8 retained the original microporous characteristics of ZIF-8 without significant structural alterations.

The pseudocapacitive behaviors of ZIF-8, GO, and G|ZIF-8 were assessed via cyclic voltammetry (CV), galvanostatic charge−discharge (GCD), and electrochemical impedance spectroscopy (EIS) by using a three-electrode cell in 1 M KOH electrolyte. The CV curves of ZIF-8 and G|ZIF-8 exhibited similar shapes (Figure 5a), indicating that graphene encapsulation did not substantially alter the intrinsic electrochemical characteristics of ZIF-8. However, the CV curve of GO exhibited distinct redox peak positions, suggesting that the electrochemical characteristics of GO were different from those of ZIF-8 and G|ZIF-8. Pairs of oxidation/reduction peak potentials were observed at 0.496 V/0.448 V for GO, 0.506 V/0.430 V for G|ZIF-8, and 0.519 V/0.448 V for ZIF-8. Comparing the intermediate values of G|ZIF-8 (0.506 V/0.430 V) with those of ZIF-8 (0.519 V/0.452 V) indicates that graphene enhances electron transport while maintaining the intrinsic electrochemical properties of ZIF-8. This slight shift suggests that partially reduced graphene decreased interfacial resistance, facilitating charge transfer without disrupting the fundamental redox behavior of ZIF-8. The GCD curves (Figure 5b) further support these observations. The GCD curves exhibited a nonlinear plateau structure, indicating pseudocapacitive electrochemical behavior.[33] At a current density of 1 A g^{-1}, the specific capacitances of GO, ZIF-8, and G|ZIF-8 were 33, 61, and 212 F g^{-1}, respectively (Table S1). The specific capacitance of G|ZIF-8 was 347% higher than that of ZIF-8. Moreover, G|ZIF-8 maintained high specific capacitance even at high current densities (Figures S10−12).

To further verify whether the enhanced electron transport in G|ZIF-8 increased the capacitance observed in the CV and GCD curves, the charge storage mechanism was quantified by separating the capacitive- and diffusion-controlled contributions (Figures 5c, 5d, S13, and S14).[34,35] In the case of G|ZIF-8, the capacitive contribution was considerably greater than that in the case of ZIF-8, whereas the diffusion-controlled contribution was similar. At each potential V and scan rate ν, the CV currents were deconvoluted using $i(V)=k_1\nu+k_2\nu^{1/2}$ to separate surface-controlled (capacitive, $k_1\nu$) and diffusion-controlled ($k_2\nu^{1/2}$) contributions; the coefficients $k_1(V)$ and $k_2(V)$ were obtained by linear regression at every V over multiple ν and then integrated over the potential window to yield the fractions at each scan rate, following established practice for pseudocapacitive systems.[36] This potentialresolved mapping avoids assuming a constant ratio and follows standard practice. Consistent with general pseudocapacitive trends, the capacitive fraction increases with ν. Distinctly, G|ZIF-8 exhibits a larger capacitive share than ZIF-8 across all ν while retaining a comparable diffusion-controlled component, which is

https://doi.org/10.1021/acsanm.5c02501
ACS Appl. Nano Mater. XXXX, XXX, XXX−XXX

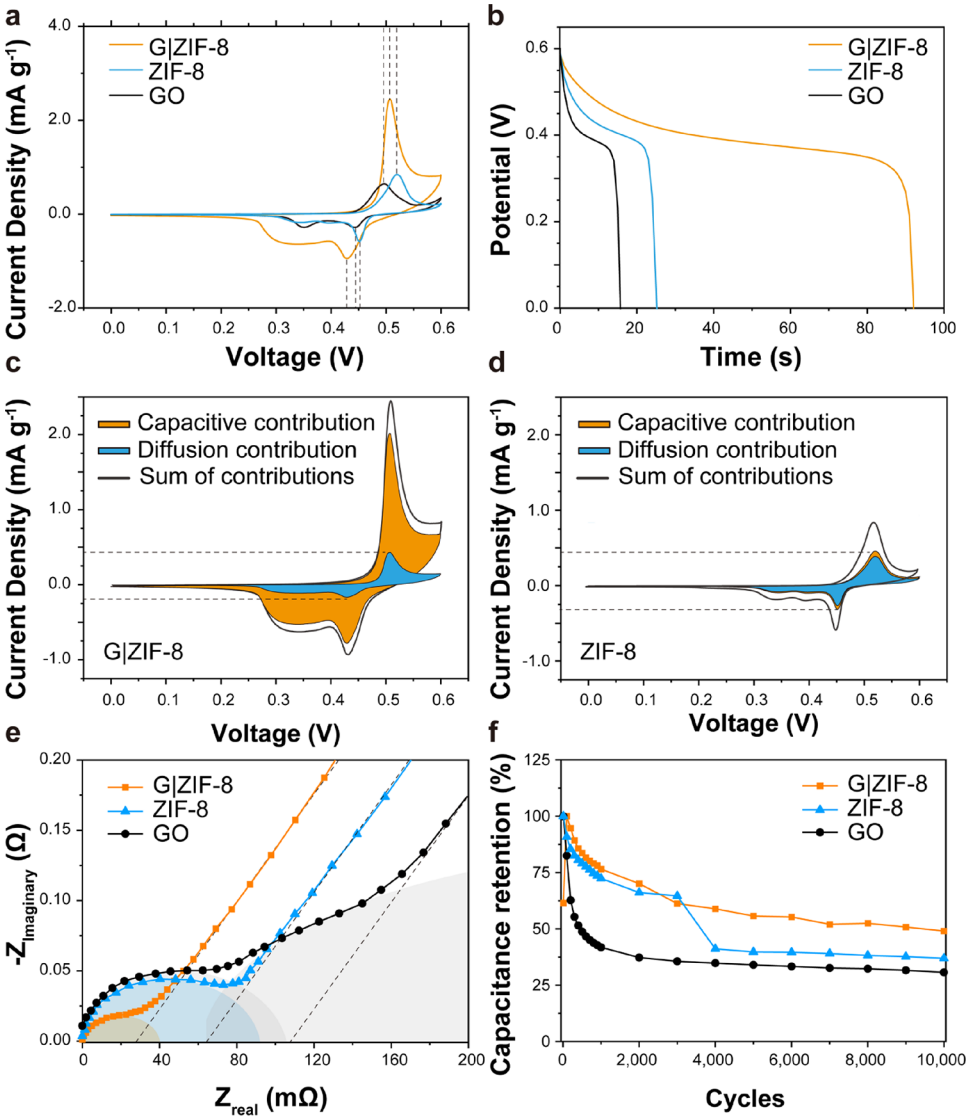

Figure 5. (a) Cyclic voltammetry curves of G|ZIF-8, ZIF-8, and GO at 1 mV s^{-1}. (b) Galvanostatic charge−discharge curves of G|ZIF-8, ZIF-8, and GO at 1 A g^{-1}. (c, d) Capacitive−diffusion contribution, obtained from the CV curves using $i(v)=k_1\nu + k_2\nu^{1/2}$, of G|ZIF-8 and ZIF-8 at 1 mV s^{-1}; (e) Nyquist plots of the GO, ZIF-8, and G|ZIF-8 electrodes; and (f) specific capacitance retention rates of GO, ZIF-8, and G|ZIF-8 over 10,000 cycles at 50 mV s^{-1}.

attributed to preserved ion-accessible microporosity.[37] For completeness, the deconvolution of GO is shown in Figure S15, where diffusion-controlled contributions (~38% at 1 mV s^{-1}) diminish rapidly at higher scan rates, reflecting sluggish ion transport through stacked GO sheets. This behavior contrasts with G|ZIF-8, where diffusion contributions are preserved despite enhanced capacitive storage.

EIS was used to assess electrical and ionic conductivities. The Nyquist plots of GO, ZIF-8, and G|ZIF-8 contained semicircles and straight lines in the high- and low-frequency regions, respectively (Figure 5e).[38] The diameters of these semicircles represent the charge-transfer resistance, R_{ct}, which indicates the ease of electron and ion transport within the electrode.[39] The R_{ct} values of GO, ZIF-8, and G|ZIF-8 were 104, 89, and 40 mΩ, respectively, indicating that the electrode resistance of G|ZIF-8 was considerably lower than those of GO and ZIF-8. In the low-frequency region, the slope of the straight line represents ion-diffusion behavior, which is associated with Warburg diffusion resistance. The nearly identical slopes of G|ZIF-8 and ZIF-8 suggest that partially reduced GO encapsulation did not impede ion mobility but rather maintained the open ion-accessible pathways.[40] This trend is consistent with the capacitive-dominated charge storage observed in Figure 5c, in which G|ZIF-8 exhibits a significantly higher capacitive contribution while retaining a similar diffusion-controlled contribution. The preservation of diffusion-controlled behavior alongside increased capacitive storage further supported the role of graphene in optimizing electron transport without blocking the micropores in G|ZIF-8. Furthermore, the Nyquist plot of GO contained two distinct semicircles, indicating the presence of additional interfacial resistance. This could be attributed to a stacking structure, which introduces charge-transfer barriers between the GO layers. By contrast, the Nyquist plot of G|ZIF-8 exhibited a single semicircle similar to that of ZIF-8, implying that graphene did not add to the interfacial resistance of G|ZIF-8. This suggests that the graphene in G|ZIF-8 was well integrated with the ZIF-8 structure, maintaining an efficient charge-

https://doi.org/10.1021/acsanm.5c02501
ACS Appl. Nano Mater. XXXX, XXX, XXX−XXX

transport pathway without adding interfacial barriers. Additionally, the Bode plot confirms these results (Figure S16). At low frequencies, the phase angle of G|ZIF-8 is the smallest, indicating a high capacitive contribution. In addition, the frequency at a phase angle of − 45° of G|ZIF-8 is 2.22 Hz, which is higher than those of ZIF-8 (1.49 Hz) and GO (0.39 Hz), suggesting that the porous structure of G|ZIF-8 was not blocked by GO layer. This indicates that G|ZIF-8 maintained the intrinsic porosity of ZIF-8 and was optimized for ion diffusion.[41,42] Consequently, graphene encapsulation preserved the intrinsic microporosity of ZIF-8, while the defects in the GO layer, which served as ion diffusion pathways, were partially reconstructed into sp2 carbon structures, thereby enhancing ionic conductivity and charge transfer efficiency, and ultimately improving capacitive performance.

The long-term cycling stabilities of GO, ZIF-8, and G|ZIF-8 were evaluated over 10,000 cycles at 50 mV s^{-1} (Figure 5f). After cycling, the capacitance retention levels were 31% for GO, 37% for ZIF-8, and 49% for G|ZIF-8, respectively, demonstrating the enhanced durability of G|ZIF-8. The CV curves recorded at different cycles (Figures S17−19) exhibited minimal peak shifts, indicating excellent electrochemical stability and consistent charge storage behavior over prolonged cycling.

3. CONCLUSION

We developed a self-assembly strategy for integrating GO with ZIF-8 to achieve uniform encapsulation while preserving the intrinsic microporous structure of ZIF-8. Unlike the conventional MOF-graphene composites that exhibit pore blockage or structural instability, GO adhered to the MOF surface without obstructing the ion-transport pathways in the composite prepared using the proposed strategy. The resulting G|ZIF-8 composite retained the high surface area and porosity of ZIF-8 while exhibiting substantially improved electron transport through enhanced interfacial interactions. Electrochemical characterization demonstrated that the specific capacitance of G|ZIF-8 was 347% higher than that of ZIF-8, charge-transfer resistance (40 mΩ) was considerably lower, and cycling stability was superior (49% capacitance retention after 10,000 cycles). These trends are consistent with the potential-resolved CV deconvolution, which shows an enhanced capacitive share while retaining a comparable diffusion-controlled component. These findings suggest that partially reduced GO encapsulation not only enhanced charge transport and cycling durability but also optimized the utilization of ZIF-8's microporous structure in energy-storage applications. Owing to its scalability and simplicity, the proposed approach can serve as a versatile platform for designing next-generation porous nanomaterials for supercapacitors, electrocatalysis, and gas separation.

4. EXPERIMENTAL METHODS

4.1. Materials. Ethyl alcohol (anhydrous, Deajung), methyl alcohol (anhydrous, Deajung), zinc nitrate hexahydrate (98%, Sigma-Aldrich), 2-methylimidazole (99%, Sigma-Aldrich), APTES (99%, Sigma-Aldrich), *N*-methylpyrrolidone (99.5%, Samchun), single-layered GO powder (H method; ACS Material), Super P (Beyond Battery), and polyvinylidene fluoride binder (HSC900, MTI Corp) were used.

4.2. Synthesis of ZIF-8. To obtain ZIF-8, 2.97 g of zinc nitrate hexahydrate and 0.82 g of 2-methylimidazole were dissolved separately in 200 mL of methanol. Subsequently, the two solutions were mixed, and the mixture was stirred for 24 h. Then, the product was washed in methanol and dried in a vacuum oven at 75 °C overnight to obtain a powder.

4.3. Synthesis of G|ZIF-8. To coat ZIF-8 (APTES|ZIF-8) with APTES, 100 mL of ethanol was added to 200 mg of ZIF-8 under sonication. Subsequently, 1 mL of APTES was added to the dispersed solution and refluxed at 90 °C for 4 h, followed by washing the product thrice with ethanol. Next, the material was dried in a vacuum oven at 75 °C overnight to obtain a powder, and 5 mL of the GO solution (0.2 mg/mL) was added to 20 mg of APTES|ZIF-8 and stirred for 30 min. After washing with deionized water, the samples were dried in an oven.

4.4. Electrode Preparation. The catalyst inks were prepared as follows. Three types of electrodes were fabricated using GO, ZIF-8, and G|ZIF-8 as the active materials, respectively. For each electrode, the active material, Super P conductive additive, and polyvinylidene fluoride (PVDF) binder were mixed in a weight ratio of 7:2:1 to form the electrode slurry. *N*-methylpyrrolidone (NMP) was used as the solvent for mixing, and the resulting slurry was uniformly coated onto Ni foam substrates. The electrodes were then dried in a vacuum oven at 100 °C for 4 h.

4.5. Structural Characterization. XRD patterns were obtained using a D8 Advance (Bruker) X-ray diffractometer operated at 40 kV and 40 mA along with Cu Kα radiation. TEM images were obtained using a JEM-ARM200F (JEOL) transmission electron microscope operated at an acceleration voltage of 200 kV. Field-emission SEM (FE-SEM) images were obtained using a JSM-7600F microscope (JEOL). FTIR spectroscopy was performed using a Nicolet IS50 FTIR spectrometer (Thermo Fisher Scientific) with powder-pressed KBr pellets and a wavenumber range of 4000−400 cm^{-1}. The BET specific surface areas and pore-size distributions were measured using a Belsorp MINI X (MicrotracBEL). XPS measurements were performed with Al Kα radiation (1486.6 eV) using a Nexsa X-ray photoelectron spectrometer (Thermo Fisher Scientific). The zeta potential values were measured using an SZ-100 particle size analyzer (Horiba).

4.6. Electrochemical Characterization. CV, GCD, and EIS tests were conducted in a three-electrode cell configuration using a potentiostat (VSP, Bio-Logic) to evaluate the supercapacitor characteristics of the prepared electrodes. The fabricated electrodes were used as the working electrodes. A Pt wire, Hg/HgO (1 M KOH), and 1 M KOH were used as the counter electrode, reference electrode, and electrolyte, respectively. The CV and GCD experiments were conducted within a voltage window of 0−0.6 V. The CV tests were conducted at scan rates between 0.5−50 mV s^{-1}. The GCD tests were conducted at current densities between 1.0−20 A g^{-1}. The EIS measurements were conducted in the frequency range of 100 kHz−0.1 Hz at an amplitude of 0.5 V.

The specific capacitance (F g^{-1}) was calculated from the GCD curves using Equation 1).[43]

$$C_s = \frac{2i_m \int V dt}{V^2 \Big|_{V_i}^{V_f}} \quad (1)$$

Here, $i_m = I/m$ (A g^{-1}) is the current density, where I is the current, m is the mass of the active material, and $\int$Vdt is the integral current area. Moreover, V denotes the potential, and its initial and final values are V_i and V_f, respectively.

■ ASSOCIATED CONTENT

Supporting Information

The Supporting Information is available free of charge at https://pubs.acs.org/doi/10.1021/acsanm.5c02501.

EDS mapping images, TEM and HRTEM images, additional XPS data for each element, Raman spectra, GCD curves at various current densities, capacitive and diffusion contribution ratios according to scan rates, Bode plot, CV curves every 2000 cycles, specific

https://doi.org/10.1021/acsanm.5c02501
ACS Appl. Nano Mater. XXXX, XXX, XXX−XXX

capacitance values derived from GCD measurements (PDF)

AUTHOR INFORMATION

Corresponding Authors

Won Ho Choi − *Department of Petrochemical Materials, Chonnam National University, Yeosu-si 59631, Republic of Korea;* orcid.org/0000-0001-6848-0379; Email: wonhochoi@jnu.ac.kr

Jeeyoung Shin − *Department of Mechanical Systems Engineering and Institute of Advanced Materials and Systems, Sookmyung Women's University, Seoul 04310, Republic of Korea;* orcid.org/0000-0002-5490-908X; Email: jshin@sookmyung.ac.kr

Authors

Bo-Min Kim − *Department of Mechanical Systems Engineering, Sookmyung Women's University, Seoul 04310, Republic of Korea;* orcid.org/0009-0005-2576-7341

Gun Woo Jang − *Department of Petrochemical Materials, Chonnam National University, Yeosu-si 59631, Republic of Korea*

Changhyun Ko − *Department of Applied Physics and Institute of Advanced Materials and Systems, Sookmyung Women's University, Seoul 04310, Republic of Korea*

Kyung Min Choi − *Institute of Advanced Materials and Systems and Department of Chemical and Biological Engineering, Sookmyung Women's University, Seoul 04310, Republic of Korea;* orcid.org/0000-0001-7181-902X

Complete contact information is available at: https://pubs.acs.org/10.1021/acsanm.5c02501

Author Contributions

B.-M.K., W.H.C., and J.S. conceptualized this idea. B.-M.K. conducted material synthesis/measurement/analysis, and G.W.J. conducted EIS measurements. C.K. and K.M.C. conducted BET measurements. B.-M.K. conducted electrochemical measurement/analysis. W.H.C. and J.S. supervised the project and wrote the manuscript with B.-M.K.

Notes

The authors declare no competing financial interest.

ACKNOWLEDGMENTS

This study was supported by the Mid-Career Researcher Program (RS-2024-00449136) and Basic Research Laboratory Program (RS-2023-00218255) through a National Research Foundation of Korea (NRF) grant funded by the Korean Government (MSIT), and by he Regional Innovation System & Education (RISE) program through the Jeollanamdo RISE center, funded by the Ministry of Education (MOE) and the Jeollanamdo, Republic of Korea. The authors would like to thank AMP and Gi-Gas for helpful discussions (2025-RISE-14-007).

ABBREVIATIONS

MOFs,Metal−organic frameworks; G|MOF,Graphene-encapsulated metal−organic framework; APTES,3-Aminopropyltriethoxysilane; 2-mim,2-Methyl imidazolate; ZIF-8,Zeolitic imidazolate framework-8; GO,Graphene oxide; SEM,Scanning electron microscope; EDS,Energy-dispersive X-ray spectroscopy; FTIR,Fourier-transform infrared; TEM,Transmission electron microscopy; XRD,X-ray diffraction; BET,Brunauer−Emmett−Teller; HK,Horvath−Kawazoe; BJH,Barrett−Joyner−Halenda; CV,Cyclic voltammetry; GCD,Galvanostatic charge−discharge; EIS,Electrochemical impedance spectroscopy; NMP,*N*-methylpyrrolidone

REFERENCES

(1) Mehek, R.; Iqbal, N.; Noor, T.; Amjad, M. Z. B.; Ali, G.; Vignarooban, K.; Khan, M. A. Metal−organic framework based electrode materials for lithium-ion batteries: a review. *RSC Adv.* **2021**, *11*, 29247−29266.

(2) Pathak, A.; et al. Integration of a (−Cu−S−) n plane in a metal−organic framework affords high electrical conductivity. *Nat. Commun.* **2019**, *10*, 1721.

(3) Sun, L.; Campbell, M. G.; Dincă, M. Electrically conductive porous metal−organic frameworks. *Angew. Chem., Int. Ed.* **2016**, *55*, 3566.

(4) Sheberla, D.; Bachman, J. C.; Elias, J. S.; Sun, C. J.; Shao-Horn, Y.; Dincă, M. Conductive MOF electrodes for stable supercapacitors with high areal capacitance. *Nat. Mater.* **2017**, *16*, 220−224.

(5) Choi, W. H.; Kim, K. H.; Lee, H.; Choi, J. W.; Park, D. G.; Kim, G. H.; Choi, K. M.; Kang, J. K. Metal-Organic Fragments with Adhesive Excipient and Their Utilization to Stabilize Multimetallic Electrocatalysts for High Activity and Robust Durability in Oxygen Evolution Reaction. *Adv. Sci.* **2021**, *8*, No. 2100044.

(6) Liang, X.; Zhang, F.; Feng, W.; Zou, X.; Zhao, C.; Na, H.; Liu, C.; Sun, F.; Zhu, G. From metal−organic framework (MOF) to MOF−polymer composite membrane: enhancement of low-humidity proton conductivity. *Chem. Sci.* **2013**, *4*, 983−992.

(7) Sathiyan, K.; Dutta, A.; Marks, V.; Fleker, O.; Zidki, T.; Webster, R. D.; Borenstein, A. Nano-encapsulation: overcoming conductivity limitations by growing MOF nanoparticles in mesoporous carbon enables high electrocatalytic performance. *NPG Asia Mater.* **2023**, *15* (1), 18.

(8) Jiang, W.; Wu, X.; Kang, P.; Zhang, Y.; Guo, H.; Yang, S.; Zheng, Q. Highly electrically conductive MOF/conducting polymer nanocomposites toward tunable electromagnetic wave absorption. *J. Mater. Sci. Technol.* **2025**, *205*, 258−269.

(9) Park, K. S.; Ni, Z.; Côté, A. P.; Choi, J. Y.; Huang, R.; Uribe-Romo, F. J.; Chae, H. K.; O'Keeffe, M.; Yaghi, O. M. Exceptional chemical and thermal stability of zeolitic imidazolate frameworks. *Proceedings of the National Academy of Sciences. Proc. Natl. Acad. Sci.* **2006**, *103*, 10186−10191.

(10) Tian, F.; Cerro, A. M.; Mosier, A. M.; Wayment-Steele, H. K.; Shine, R. S.; Park, A.; Webster, E. R.; Johnson, L. E.; Johal, M. S.; Benz, L. Surface and Stability Characterization of a Nanoporous ZIF-8 Thin Film. *J. Phys. Chem. C* **2014**, *118*, 14449−14456.

(11) Miranda, A.; Martínez, L.; De Beule, P. A. Facile synthesis of an aminopropylsilane layer on Si/SiO_2 substrates using ethanol as APTES solvent. *MethodsX* **2020**, *7*, No. 100931.

(12) Sypabekova, M.; Hagemann, A.; Rho, D.; Kim, S. 3-Aminopropyltriethoxysilane (APTES) deposition methods on oxide surfaces in solution and vapor phases for biosensing applications. *Biosensors* **2023**, *13* (1), 36.

(13) Kang, H.; Lee, J.; O'Keefe, T.; Tuga, B.; Hogan, C. J., Jr.; Haynes, C. L. Effect of (3-aminopropyl)triethoxysilane on dissolution of silica nanoparticles synthesized via reverse microemulsion. *Nanoscale* **2022**, *14* (25), 9021−9030.

(14) Jongert, T. K.; Slowinski, I. A.; Dao, B.; Cortez, V. H.; Gredig, T.; Plascencia, N. D.; Tian, F. Zeta potential and size analysis of zeolitic imidazolate framework-8 nanocrystals prepared by surfactant-assisted synthesis. *Langmuir.* **2024**, *40*, 6138−6148.

(15) Li, D.; Müller, M. B.; Gilje, S.; Kaner, R. B.; Wallace, G. G. Processable aqueous dispersions of graphene nanosheets. *Nat. Nanotechnol.* **2008**, *3*, 101−105.

(16) Molčanov, K.; Stare, J.; Kojić-Prodić, B.; Lecomte, C.; Dahaoui, S.; Jelsch, C.; Wenger, E.; Šantić, A.; Zarychta, B. A polar/π model of interactions explains face-to-face stacked quinoid rings: a case study of

https://doi.org/10.1021/acsanm.5c02501
ACS Appl. Nano Mater. XXXX, XXX, XXX−XXX

the crystal of potassium hydrogen chloranilate dihydrate. *CrystEngComm.* **2015**, *17*, 8645−8656.
(17) Ding, M.; Inoue, T.; Enriquez, J. I.; Halim, H. H.; Ogawa, Y.; Taniyasu, Y.; Hamamoto, Y.; Morikawa, Y.; Kobayashi, Y. Reduction of interlayer interaction in multilayer stacking graphene with carbon nanotube insertion: Insights from experiment and simulation. *J. Phys. Chem. C* **2023**, *127*, 23768−23777.
(18) Pokhrel, J.; Bhoria, N.; Anastasiou, S.; Tsoufis, T.; Gournis, D.; Romanos, G.; Karanikolos, G. N. CO_2 adsorption behavior of amine-functionalized ZIF-8, graphene oxide, and ZIF-8/graphene oxide composites under dry and wet conditions. *Microporous Mesoporous Mater.* **2018**, *267*, 53−67.
(19) Li, S.; Zhang, Z.; Yuan, F.; Wang, Z.; Wang, B. Balancing interlayer spacing, pore structures and conductivity endows hard carbon with high capacity for rechargeable aluminum batteries. *Phys. Chem. Chem. Phys.* **2024**, *26* (23), 16838−16846.
(20) Song, J.; Wang, X.; Chang, C.-T. Preparation and characterization of graphene oxide. *J. Nanomater.* **2014**, *2014*, No. 276143.
(21) Guo, L.; et al. Two-beam-laser interference mediated reduction, patterning and nanostructuring of graphene oxide for the production of a flexible humidity sensing device. *Carbon.* **2012**, *50*, 1667−673.
(22) Shin, Y. E.; Sa, Y. J.; Park, S.; Lee, J.; Shin, K. H.; Joo, S. H.; Ko, H. An ice-templated, pH-tunable self-assembly route to hierarchically porous graphene nanoscroll networks. *Nanoscale.* **2014**, *6*, 9734−9741.
(23) Tian, F.; Cerro, A. M.; Mosier, A. M.; Wayment-Steele, H. K.; Shine, R. S.; Park, A.; Webster, E. R.; Johnson, L. E.; Johal, M. S.; Benz, L. Surface and stability characterization of a nanoporous ZIF-8 thin film. *J. Phys. Chem. C* **2014**, *118*, 14449−14456.
(24) Martin, H. J.; Schulz, K. H.; Bumgardner, J. D.; Walters, K. B. XPS study on the use of 3-aminopropyltriethoxysilane to bond chitosan to a titanium surface. *Langmuir.* **2007**, *23*, 6645−6651.
(25) Johra, F. T.; Jung, W. G. Hydrothermally reduced graphene oxide as a supercapacitor. *Appl. Surf. Sci.* **2015**, *357*, 1911−1914.
(26) Eckmann, A.; Felten, A.; Mishchenko, A.; Britnell, L.; Krupke, R.; Novoselov, K. S.; Casiraghi, C. Probing the nature of defects in graphene by Raman spectroscopy. *Nano Lett.* **2012**, *12*, 3925−3930.
(27) Liu, L.; Zhang, L.; Li, Y.; Wen, S.; Yu, Z.; Mao, Y.; Zhi, X. γ-Aminopropyl triethoxysilane functionalized graphene oxide for composites with high dielectric constant and low dielectric loss. *Compos. Part A Appl. Sci. Manuf.* **2015**, *76*, 194−202.
(28) Lopez-Diaz, D.; Delgado-Notario, J. A.; Clericò, V.; Diez, E.; Merchan, M. D.; Velázquez, M. M. Towards understanding the Raman spectrum of graphene oxide: the effect of the chemical composition. *Coatings* **2020**, *10* (6), 524.
(29) López-Díaz, D.; López Holgado, M.; García-Fierro, J. L.; Velázquez, M. M. Evolution of the Raman spectrum with the chemical composition of graphene oxide. *J. Phys. Chem. C* **2017**, *121*, 20489−20497.
(30) Deacon, A.; Briquet, L.; Malankowska, M.; Massingberd-Mundy, F.; Rudić, S.; Hyde, T. I.; Cavaye, H.; Coronas, J.; Poulston, S.; Johnson, T. Understanding the ZIF-L to ZIF-8 transformation from fundamentals to fully costed kilogram-scale production. *Commun. Chem.* **2022**, *5*, 18.
(31) Ambroz, F.; Macdonald, T. J.; Martis, V.; Parkin, I. P. Evaluation of the BET Theory for the Characterization of Meso and Microporous MOFs. *Small Methods* **2018**, *2*, No. 1800173.
(32) Kuila, U.; Prasad, M. Specific surface area and pore-size distribution in clays and shales. *Geophys. Prospect.* **2013**, *61*, 341−362.
(33) Chodankar, N. R.; Pham, H. D.; Nanjundan, A. K.; Fernando, J. F. S.; Jayaramulu, K.; Golberg, D.; Han, Y.-K.; Dubal, D. P. True meaning of pseudocapacitors and their performance metrics: asymmetric versus hybrid supercapacitors. *Small.* **2020**, *16*, No. 2002806.
(34) Wang, J.; Polleux, J.; Lim, J.; Dunn, B. Pseudocapacitive contributions to electrochemical energy storage in TiO2 (anatase) nanoparticles. *J. Phys. Chem. C* **2007**, *111*, 14925−14931.
(35) Pervez, S.; Iqbal, M. Z. Capacitive and Diffusive Contributions in Supercapacitors and Batteries: A Critique of b-Value and the $\nu-\nu1/2$ Model. *Small.* **2023**, *19*, No. 2305059.
(36) Hu, Z.; Zhu, Z.; Cheng, F.; Zhang, K.; Wang, J.; Chen, C.; Chen, J. Pyrite FeS2 for high-rate and long-life rechargeable sodium batteries. *Energy Environ. Sci.* **2015**, *8*, 1309.
(37) Yan, L.; et al. Regulating the specific surface area and porous structure of carbon for high performance supercapacitors. *Appl. Surf. Sci.* **2023**, *615*, No. 156267.
(38) Mei, B. A.; Munteshari, O.; Lau, J.; Dunn, B.; Pilon, L. Physical interpretations of Nyquist plots for EDLC electrodes and devices. *J. Phys. Chem. C* **2018**, *122*, 194−206.
(39) Lazanas, A. C.; Prodromidis, M. I. Electrochemical impedance spectroscopy— a tutorial. *ACS Meas. Sci. Au* **2023**, *3*, 162−193.
(40) Li, Y.; Kim, J.; Wang, J.; Liu, N. L.; Bando, Y.; Alshehri, A. A.; Yamauchi, Y.; Hou, C. H.; Wu, K. C. W. High performance capacitive deionization using modified ZIF-8-derived, N-doped porous carbon with improved conductivity. *Nanoscale* **2018**, *10*, 14852−14859.
(41) Kar, K. K. *Handbook of nanocomposite supercapacitor materials II*; Springer Cham: Cham, Switzerland, 2020.
(42) Ding, R.; Qi, L.; Jia, M.; Wang, H. Facile and large-scale chemical synthesis of highly porous secondary submicron/micron-sized NiCo2O4 materials for high-performance aqueous hybrid AC-NiCo2O4 electrochemical capacitors. *Electrochim. Acta* **2013**, *107*, 494−502.
(43) Mai, L. Q.; Minhas-Khan, A.; Tian, X.; Hercule, K. M.; Zhao, Y. L.; Lin, X.; Xu, X. Synergistic interaction between redox-active electrolyte and binder-free functionalized carbon for ultrahigh supercapacitor performance. *Nat. Commun.* **2013**, *4*, 2923.

https://doi.org/10.1021/acsanm.5c02501
ACS Appl. Nano Mater. XXXX, XXX, XXX−XXX